ADVANCED MATERIALS
www.advmat.de

Architected Lattices with High Stiffness and Toughness via Multicore–Shell 3D Printing

Jochen Mueller, Jordan R. Raney, Kristina Shea, and Jennifer A. Lewis**

The ability to create architected materials that possess both high stiffness and toughness remains an elusive goal, since these properties are often mutually exclusive. Natural materials, such as bone, overcome such limitations by combining different toughening mechanisms across multiple length scales. Here, a new method for creating architected lattices composed of core–shell struts that are both stiff and tough is reported. Specifically, these lattices contain orthotropic struts with flexible epoxy core–brittle epoxy shell motifs in the absence and presence of an elastomeric silicone interfacial layer, which are fabricated by a multicore–shell, 3D printing technique. It is found that architected lattices produced with a flexible core-elastomeric interface-brittle shell motif exhibit both high stiffness and toughness.

Despite recent advances in the design and fabrication of lightweight materials,[1–7] the ability to create architectures that possess both high stiffness and toughness remains an elusive goal as these properties are often mutually exclusive.[8] Natural materials overcome such limitations by combining different toughening mechanisms across multiple length scales. In bone, for example, fibrillary sliding occurs on the nanometer scale,[9,10] while crack bridging and deflection happen at length scales ranging from tens to hundreds of micrometers.[11,12] Architected materials are an emerging class of matter in which the distribution of multiple materials (including porosity) is engineered for mechanical performance.[13–16] To date, several periodic lattices have been fabricated with high specific stiffness and strength,[2,16–18] including honeycombs,[3] woodpiles with solid[4,19] and foam struts,[5,20] and octet trusses with solid[21,22] and hollow struts.[1,2,23–25]

To enhance fracture toughness, energy absorbing mechanisms that increase the length over which a critical crack must propagate prior to failure are needed.[26,27] For example, nacre, a natural composite with a brick-and-mortar architecture, exhibits high fracture toughness that arises when cracks are deflected around rigid aragonite "bricks," while being bridged by thin, compliant organic "mortar."[28] However, it is difficult to introduce this type of mechanism into lattice architectures, since complex struts are challenging to build.[8,29] While hierarchical lattices (≈1 mm^3) composed of an octet truss geometry with octet truss-based struts have recently been constructed using two-photon polymerization,[6] those architectures are unable to confer both high stiffness and toughness.[5,6,20,30]

Here, we report a new method for creating architected lattices composed of core–shell (C–S) struts that are both stiff and tough. Specifically, these lattices contain orthotropic struts with flexible epoxy core–brittle epoxy shell motifs in the absence and presence of an elastomeric silicone interfacial layer. We explore the effects of strut composition, i.e., C–S versus core–interface–shell (C–I–S), core-to-shell ratio (d/D), and interface thickness on their stiffness, strength, and fracture toughness. These structures are produced by direct ink writing,[31] an extrusion-based 3D printing technique, in which viscoelastic epoxy inks are deposited through a given nozzle in a layerwise manner and subsequently cured. To pattern the desired structures, we designed and fabricated multicore–shell printheads for coextrusion of coaxially aligned epoxy and silicone resins (**Figure 1**a,b). The tapered nozzles are created in a reproducible manner using stereolithography (Figure S1, Supporting Information), which ensures uniform flow of these inks without clogging (Figure 1b–e). The ink reservoirs are connected to the multicore–shell nozzle via a Luer lock that is directly fabricated with the nozzle. The inner channels of each printhead are retracted to decouple the minimum printable strut size from the number of input channels, therefore maximizing the feature resolution (Figure 1f). Importantly, our multicore–shell nozzles allow one to seamlessly switch individual input channels on and off, and thereby vary both the strut composition and geometry on demand, while maintaining a constant outer strut diameter (Figure 1g).

Next, we developed three viscoelastic inks based on flexible epoxy (core), brittle epoxy (shell), and silicone-based

J. Mueller, Prof. K. Shea
Department of Mechanical and Process Engineering
Engineering Design and Computing Laboratory
ETH Zurich
8092 Zurich, Switzerland
E-mail: kshea@ethz.ch
Prof. J. R. Raney
Mechanical Engineering and Applied Mechanics
University of Pennsylvania
Philadelphia, PA 19104, USA
Prof. J. A. Lewis
John A. Paulson School of Engineering and Applied Sciences
Wyss Institute for Biologically Inspired Engineering
Harvard University
Cambridge, MA 02138, USA
E-mail: jalewis@seas.harvard.edu
The ORCID identification number(s) for the author(s) of this article can be found under https://doi.org/10.1002/adma.201705001.

DOI: 10.1002/adma.201705001

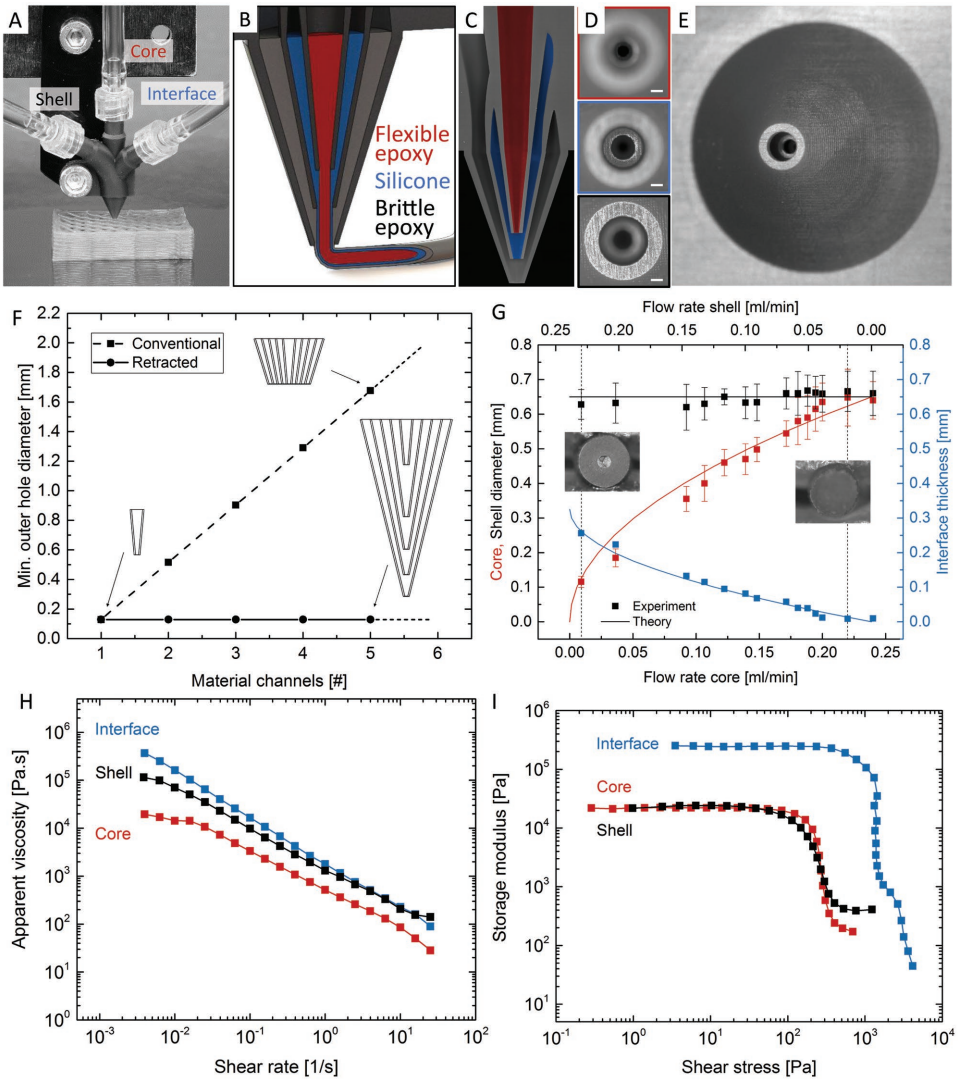

Figure 1. Multicore–shell nozzles and ink rheology. a) Optical image of the coaxial printhead connected to the core, interface, and shell ink reservoirs. b) Schematic cross-sectional view of the C–S printhead and c) corresponding false-colored optical image of the C–S nozzle from which the flexible epoxy core (red), elastomeric silicone interface (blue), and brittle epoxy shell (gray) inks are coextruded. d,e) End-on views of these C–S nozzles, in which the retracted inner channels enable higher resolution compared with conventional designs. f) Plot of outer nozzle diameter as a function of number of coaxial materials printed by these multicore–shell printheads, which clearly demonstrates the advantage of the retracted design. g) Using a multicore–shell printhead, one can systematically vary the *d*/*D* ratio and interfacial layer thickness while maintaining the outer diameter of the printed filamentary struts. h,i) Log–log plot of apparent viscosity as a function of shear rate and storage modulus as a function of shear stress for the flexible epoxy core (red), elastomeric silicone interface (blue), and brittle epoxy shell (gray) inks, respectively. [Scale bars = 200 µm].

(interface) resins for printing both individual architected struts and the desired 3D lattices. Each of these inks must exhibit shear thinning behavior to facilitate their flow through these nozzles under an applied pressure as well as an appropriate storage modulus, G', and shear yield stress, τ_y, to retain their extruded cylindrical shape after the C–S and C–I–S filamentary struts exit the nozzle. These requirements are identical for the single material, C–S, and C–I–S struts. The flexible core ink is based on an epoxy resin (Epon 872) that contains both fumed silica (diameter < 1 µm, 18% by weight) and rubber particles (diameter = 150 nm, 4% by weight) that modify the ink rheology and increase the stiffness and fracture toughness after curing.[32] A difunctional primary amine (12% by weight) is used as the curing agent. The brittle shell ink is based on a different epoxy resin (Epon 826) that contains nanoclay platelets (10 nm length, 1 nm thickness, 45% by weight), which serve as a rheological modifier. In this ink, an imidazole-based ionic liquid (5% by weight) is used as a curing agent, which provides a long pot life (≈30 d).[3] Finally, the interfacial layer ink consists of a silicone elastomer (10:1 by weight ratio with the catalyst). The apparent viscosity and shear moduli of the core, shell, and interfacial layer inks are provided in Figure 1h,i, respectively. Each ink is strongly shear thinning with an apparent viscosity of roughly 10^3 Pa s at a shear rate of 1 s^{-1}. Both epoxy-based inks exhibit nearly identical plateau storage moduli ($G' \approx 2 \times 10^4$ Pa) and shear yield stresses ($\tau_y \approx$ 100 Pa), while the silicone-based

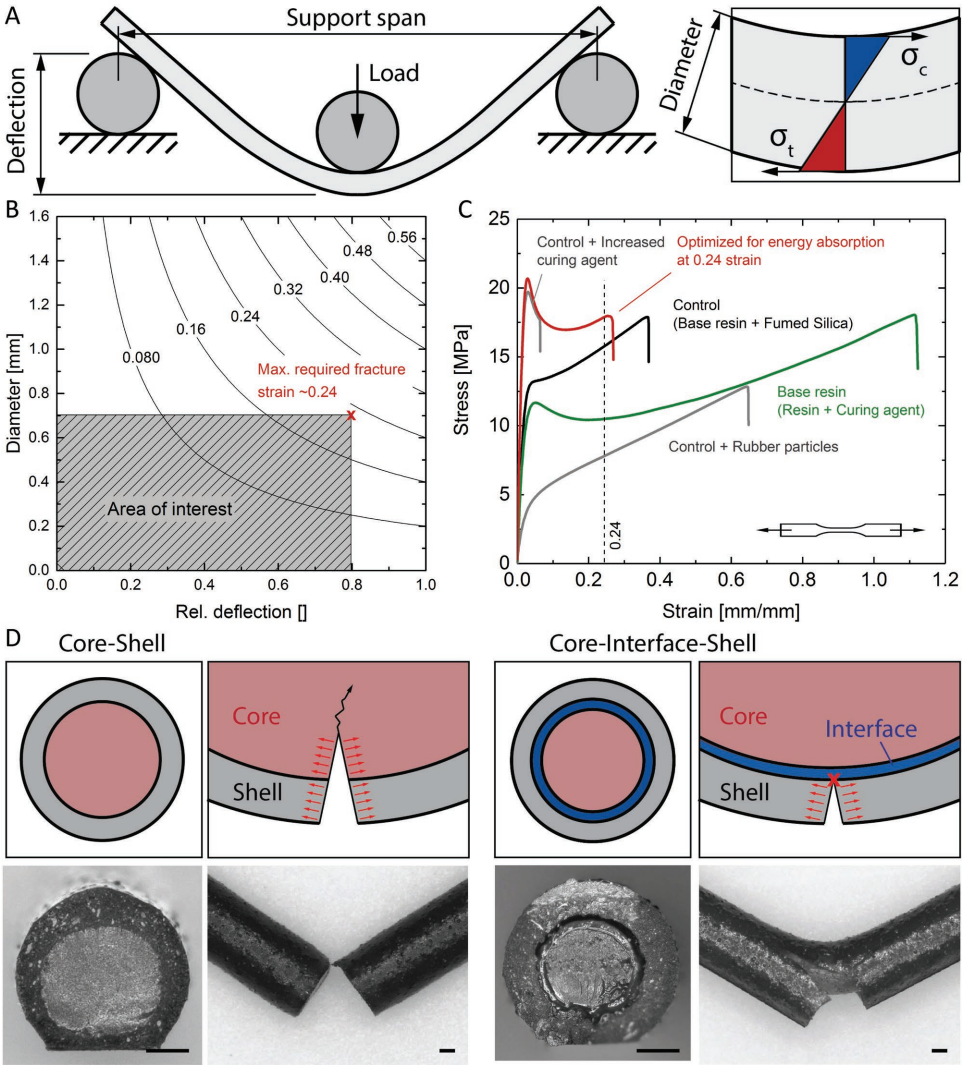

Figure 2. C–S strut design and properties. Each strut is composed of a brittle epoxy shell that provides stiffness and a flexible core that provides toughness. The modulus of a strut increases with its overall diameter to the power of four. To prevent catastrophic failure, a specific fracture strain that is dependent on the diameter and deflection is required for each design. a) Schematic view of three-point bend test and corresponding stress profile across the strut. b) Calculated dependence of strut diameter on relative deflection for different values of fracture strain, which denotes that predicted value of maximum required fracture strain. c) Stress–strain behavior for different materials tested, including the optimized combination (denoted by the red curve) that maximizes the energy absorption for the computed strain of $\varepsilon = 0.24$. d) Schematic illustrations of the C–S and C–I–S struts (cross-sectional and side views), which shows that the elastomeric interfacial layer mitigates crack propagation from the brittle epoxy shell to the flexible epoxy core. [Scale bars = 200 μm].

ink exhibits G' and τ_y values that are roughly an order of magnitude higher. Importantly, the printed features remain structurally stable during initial curing at ≈100 °C for an extended time period (>15 h).

The stiff epoxy ink is confined to the outer shell, since the stiffness of these 3D printed lattices exhibits a strong power law dependence on strut diameter, $K \propto d^4$. The flexible epoxy ink is optimized such that the core exhibits both high-energy absorption and compatibility with the shell material. To prevent catastrophic failure of the core, a fracture strain larger than the strain that occurs in every part of the structure is required (**Figure 2**a). However, the higher the fracture strain, the lower the stiffness and strength.[11] Hence, the fracture strain of the flexible epoxy core should only be marginally higher than required minimum failure strain, ε_f. To determine this value, we fixed the maximum strut diameter, d, to 0.7 mm and used a typical strut deflection, δ, in a bending-dominated lattice of 80% of span length, L, before densification, as given by

$$\varepsilon_f = \frac{6\delta d}{L^2} \tag{1}$$

Since this equation does not consider nonlinearities, the calculated minimum ε_f of 0.24 (Figure 2b) should be viewed solely as an approximation for our experimental system.

We first quantified the mechanical properties of each epoxy material by fabricating dogbone specimens and subjecting them to tensile testing. The effects of a broad range of fillers on their mechanical performance are shown in Figure 2c. Specimens composed of the base resin (pure resin with curing agent) exhibit an elastic modulus of 0.6 GPa, a tensile strength of 12 MPa, and a fracture strain of 1.1, the latter of which is well above the targeted requirement. Upon adding fumed silica or increasing the curing agent, both their stiffness and strength are increased, while their fracture strain is reduced. By contrast, the addition of rubber particles reduced each of these properties. By adjusting the filler composition and relative ratios, we produced a flexible epoxy ink with the requisite fracture strain of 0.26, which maximizes the energy absorption through a (relatively) high stiffness and strength of 1.25 GPa and 22 MPa, respectively.

We printed individual struts composed of the brittle shell-flexible core epoxy in the absence and presence of the elastomeric interlayer and characterized their mechanical properties in three-point bending to isolate boundary effects. The interfacial layer thickness (average value = 34 ± 18 μm) is kept as thin as possible while ensuring reliable separation of the core and shell. We find that the C–S struts fail completely upon crack formation, while the C–I–S struts remain partially intact (Figure 2d). In the absence of the interfacial layer, diffusion between the brittle and flexible epoxy inks within the printed C–S struts may give rise to an interfacial zone, in which there is a continuous transition in mechanical properties that could slow down and eventually halt crack propagation.[33,34] However, this is counterbalanced by the strong interfacial bonding between the brittle and flexible epoxy materials that clearly allows stress to be readily transferred from the shell to the core. By contrast, the presence of an elastomeric interfacial layer introduces a compliant region between the two epoxy materials within the individual C–I–S struts that reduces their overall stiffness. While the ideal interlayer does not either bond to the core or shell epoxy material, it provides structural stability and gives rise to a high coefficient of friction with both the core and shell materials that lead to the above observations.

Next, we fabricated C–S struts of varying d/D ratios and compared their mechanical behavior to struts made from the individual epoxy materials as well as to the C–I–S struts (**Figure 3**a–c). We find that both the pure brittle epoxy strut (d/D = 0) and the C–S struts fail completely (Figure 3a left, Figure 3b). By contrast, the flexible epoxy remains intact both in the pure flexible epoxy strut (d/D = 1, Figure 3a right) and C–I–S struts (Figure 3c). Importantly, the C–I–S struts fail in qualitatively different ways depending on the ratio d/D, e.g., when d/D = 0.4, the crack travels straight through the brittle material (Figure 3c left), while when d/D = 0.85, the crack is deflected and bifurcated multiple times (Figure 3c right, Figure 3d). Since C–S struts are expected to have some interdiffusion between layers, we used nanoindentation to measure the transition region between the brittle and flexible phases (Figure 3e,f). The brittle epoxy shell is mostly unaffected, while the flexible epoxy core exhibits an increased stiffness near the interface that linearly decreases toward the value of 1.3 GPa for the pure material at a distance of ≈400 μm from the interface.

Figure 3g highlights representative load–displacement curves obtained for individual struts of varying composition and d/D ratios, while Figure 3h shows the full set of effective modulus, ultimate tensile strength (UTS), and energy absorption data obtained for these struts with d/D values from 0 to 1, i.e., from purely brittle to purely flexible epoxy, respectively. The modulus, calculated by a least-squares fit of the initial slope of the stress–strain curves, for both the C–S and C–I–S struts initially plateaus at around 6 GPa, close to the value measured for the brittle epoxy. As d/D increases to ≈0.85, the modulus of the C–S struts remains nearly constant, while that of the C–I–S struts decreases to ≈4 GPa. Notably, as the d/D ratio increases, there is a concomitant increase in cross-sectional area of the interfacial layer. Importantly, there is good agreement with the measured values, when these effects are included in the beam theory for the flexural modulus

$$E_{\mathrm{f}} = \frac{FL^3}{48\delta I} \tag{2}$$

where F is the load, L is the span length, δ is the deflection, and I is the second moment of area of the cross-section. In Equation (2), the second moment of area, I, for a rod with circular and ring cross-sections of outer radius, R, and inner radius, r, is given by

$$I_{\mathrm{circle}} = \frac{\pi}{4} R^4,\ I_{\mathrm{ring}} = \frac{\pi}{4}\left(R^4 - r^4\right) \tag{3}$$

Using I for the core, shell, and the total filament allows one to calculate the combined Young's modulus for each d/D ratio as given by

$$E_{\mathrm{comb}} = \frac{I_{\mathrm{core}}E_{\mathrm{core}} + I_{\mathrm{shell}}E_{\mathrm{shell}}}{I_{\mathrm{comb}}} \tag{4}$$

The larger deviations observed for the C–I–S struts are due to additional measurement, analysis, and rounding errors. For the UTS, the trend is similar, i.e., the plateau value of both types of struts is ≈135 MPa at d/D = 0, while values of ≈100 MPa (C–S strut) and ≈60 MPa (C–I–S strut) are observed at d/D = 0.85. The energy absorption of the C–S and C–I–S struts is affected by their respective modulus and UTS values at a given d/D. When $0 \le d/D < 0.6$, there is little difference in energy absorption (≈3 MPa) observed between the two types of struts. At d/D = 0.6, the energy absorption of the C–S and C–I–S struts is still similar, despite the lower stiffness and strength of the latter. This observation is likely due to the fact that the flexible core within the C–I–S strut remains intact after the shell fractures, while the C–S strut fractures completely. When $d/D > 0.6$, the increasing influence of the flexible core reduces the total stiffness and strength of the C–S struts, and hence their energy absorption. Upon initiation, the crack travels through the entire strut, even those with large cores (Figure 3b). By contrast, the opposite effect is observed for the C–I–S struts at $d/D \ge 0.6$. Importantly, when $d/D \approx 0.85$, their energy absorption more than doubles above the base value of 3 MPa since their shell now fractures in a piecewise manner, as seen Figure 3c. Crack deflection and bifurcation are known to increase the

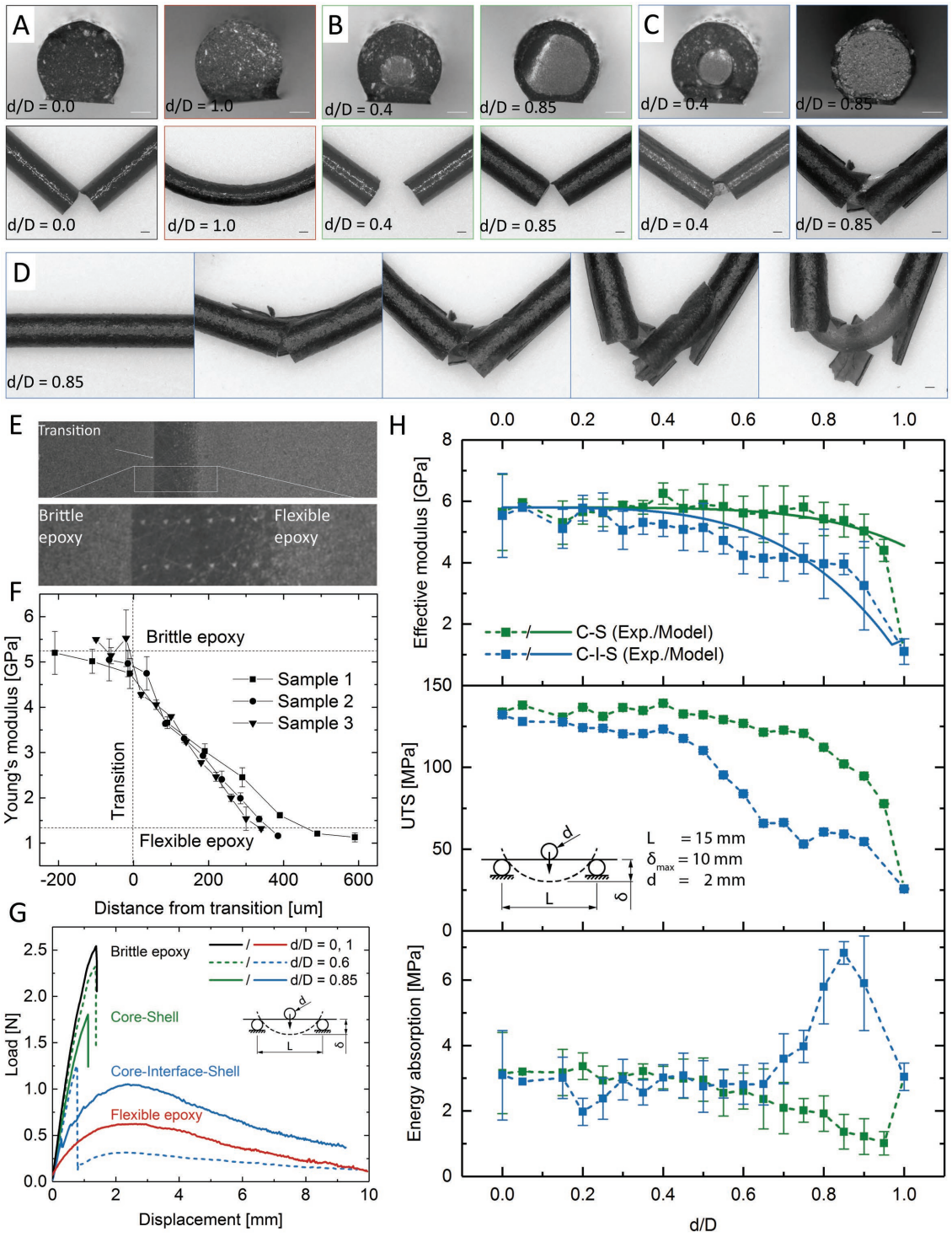

Figure 3. Mechanical properties of individual struts. a) A brittle and elastic behavior is observed for struts composed solely of the shell and core materials, respectively. b) While the C–S struts also fail from brittle fracture, c) the C–I–S struts are able to stop the crack propagation into their core. The shell layer of struts with a small core (left) fails completely, while those with a large core fail piecewise. d) A sequence of the crack propagation in a C–I–S strut with increasing strain from left to right. e,f) In the absence of the interfacial layer, diffusion occurs between the C–S epoxy layers during printing and curing, as reflected by graded interfacial zone (≈400 µm thick) and corresponding decrease in Young's modulus from the brittle epoxy shell to the flexible epoxy core. g) Load–displacement response for representative struts of varying composition and d/D ratio. h) Plots of effective modulus, UTS, and energy absorption measured for individual C–S and C–I–S struts of varying d/D ratio, which reveals the pronounced rise in energy absorption for C–I–S struts with a $d/D \approx 0.85$. The model is based on Equations (1)–(4). [Scale bars = 200 µm].

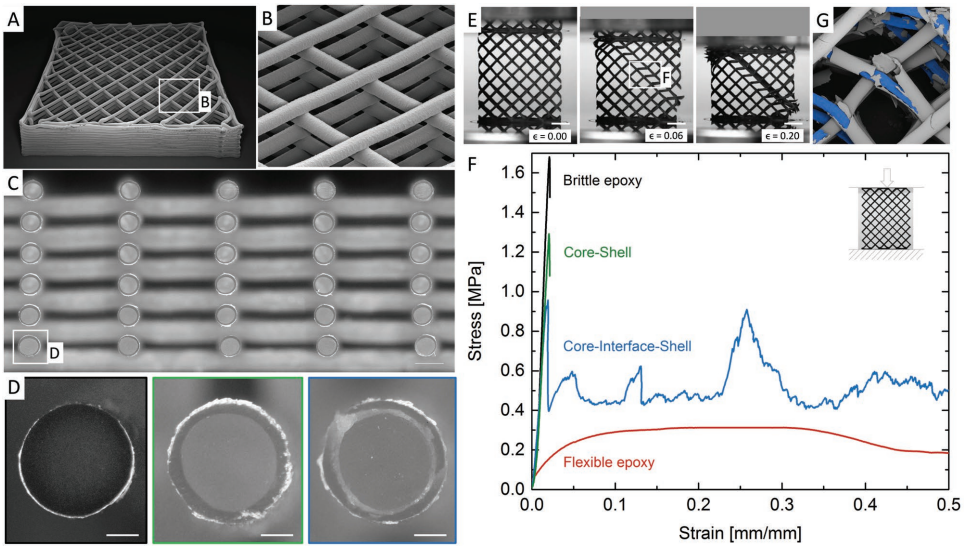

Figure 4. Architected lattices. a–c) Optical images of a representative lattice fabricated by multicore–shell direct ink writing, where a) tilted view of the entire lattice, b) closer view of printed struts, which span gaps across underlying features within the lattice, and c) cross-sectional view of the lattice composed of C–I–S struts [scale bar = 1 mm]. d) higher magnification images of exemplary brittle (black, left), C–S (green, center), and C–I–S (blue, right) struts [scale bars = 0.2 mm]. e) Optical images of a C–I–S lattice under different compression states that show a layer wise failure, typical for elastoplastic materials of this unit cell type [scale bars = 8 mm]. f) stress–strain curves for the previously shown C–I–S lattice compared with lattices composed of brittle epoxy, flexible epoxy, and C–S struts, as shown in (D). g) The interfacial layer stops crack propagation through the strut cores (false-colored blue), causing the shell to fracture into many pieces.

energy absorption due to the creation of new surfaces, especially in particulate-filled media.[35] This is reflected in the corresponding stress–strain curve by multiple small decreases associated with graceful failure. Under these conditions, the shell continues to retain stability even after multiple cracks form, which absorb additional energy.[36] Similar behavior is observed in natural composites, such as bone[37,38] and nacre,[39] as well as alumina-PMMA composites,[11] in which these composite systems perform better than the individual constituent materials.

To create 3D architected lattices, we use direct ink writing to produce bending dominated woodpile structures[40] composed of either spanning C–S or C–I–S struts. As controls, we also printed 3D lattices composed of pure brittle and flexible epoxy struts (**Figure 4**a–d). Upon curing, the connections are rigid and prevent free rotation of the struts, causing applied loads to induce bending moments that exploit the struts' energy absorption capabilities.[41] Solid walls are printed to provide structural stability during the printing and curing process. However, the walls are removed after curing to avoid boundary effects during mechanical loading. All lattices are compressed and the results normalized by their relative density. In the C–I–S lattices, layers fail along one diagonal first, followed by the collapse of the inverse diagonal layers (Figure 4e)—a behavior typical for elastoplastic materials of this unit cell type. As before, the shells fracture into pieces while the core remains intact (Figure 4f). Unlike the C–I–S-based lattices, both the brittle epoxy and C–S lattices fully collapse (Figure 4g), releasing enough energy to catapult them out of the testing apparatus. By contrast, the flexible epoxy lattices do not fail catastrophically and exhibit global out-of-plane buckling when $\varepsilon \geq 0.3$ due to the specific lattice dimensions tested. Importantly, the C–I–S lattices demonstrate superior energy absorption capabilities. Similar to the data obtained for individual struts, the modulus of the C–I–S lattices is slightly lower relative to the brittle epoxy and C–S lattices, though significantly higher than that of the flexible epoxy lattices.

In summary, we have printed architected lattices composed of multicore–shell struts that simultaneously possess high stiffness and toughness. By creating multiple printable materials and tailored coaxial nozzles, we have demonstrated that 3D structures with well-controlled strut composition and geometry can be designed and printed by multicore–shell direct ink writing. Our approach could readily be extended to more complex strut designs and lattice geometries for use in structural applications that require simultaneous optimization of weight and mechanical performance.

Experimental Section

Materials: The flexible core and brittle shell epoxy inks were prepared by mixing batches of 10–60 g of Epon 826 or Epon 872 (Momentive Performance Materials Inc., Waterford, NY, USA) with dimethyl methyl phosphonate or xylene (Sigma Aldrich, St. Louis, MO, USA) in "max 100" and "max 200" containers (FlakTek Ink, Landrum, SC, USA). The nanoclay platelets (Nanocar 1.34 TN, Southern Clay Products, Inc., Gonzales, TX, USA), fumed silica (CAB-O-SIL TS-530, Cabot Corporation, Alpharetta, GA, USA), and rubber (Hypro 1300 × 8 CTBN Emerald Performance Materials, LLC, Vancouver, WA, USA) were added stepwise, followed by mixing in vacuum (20 Torr) in a DAC 600 VAC speed mixer after each step (90 s at 800 rpm, 90 s at 1600 rpm, and 120 s at 2000 rpm, FlakTek). After allowing the inks to cool to room temperature, the Basionics VS03 (BASF, Ludwigshafen, Germany) or Epikure 3230 curing agents (Momentive Performance Materials Inc.) were added and then mixed for 30 s at 800 rpm, 30 s at 1600 rpm, and 60 s at 2000 rpm. For the interfacial layer ink, SE1700 (Dow Corning,

Midland, MI, USA) was mixed with the catalyst at a 10:1 ratio for 120 s at 2000 rpm. A summary of the constituents used for each ink is provided in Table S1 in the Supporting Information.

Ink Rheology: The rheological properties of each ink were characterized under ambient conditions using a controlled-stress rheometer (Discovery HR3, TA Instruments, New Castle, DE, USA) equipped with a 40 mm flat parallel plate geometry. Prior to rheological characterization, all inks were prepared the same way as they were for printing and carefully placed on the plate using a spatula. For the flexible core and interfacial inks, a gap distance of 500 µm was used. For the brittle shell ink, a gap distance of 1 mm was used in addition to a solvent trap to prevent solvent loss. The rheological properties of both the base epoxy resins (Figure S3, Supporting Information) and their corresponding ink formulations (Figure S4, Supporting Information) were characterized by viscometry measurements, carried out over shear rates from 0.01 to 100 s^{-1}, and oscillatory measurements carried out at a frequency of 1 Hz within the shear stress range of 0.1–3000 Pa.

Multicore–Shell Printheads: The printheads were fabricated on an Aureus Plus 3D printer using HTM140 material (EnvisionTEC, Dearborn, MI, USA) with a layer height of 50 µm and an X–Y resolution of 43 µm.

3D Printing: The core, shell, and interfacial inks were loaded into Luer lock syringe barrels of 10 or 30 mL (Nordson EFD, East Providence, RI, USA) and centrifuged for 8 min at 2200 rpm to remove the bubbles from the ink. The multicore–shell printhead was mounted on an Aerotech 3-axis stage (Aerotech, Inc., Pittsburgh, PA, USA) and connected to the loaded syringes through the Luer locks. Ink extrusion was controlled by an Ultimus V pressure pump (core, Nordson EFD), a PHD Ultra syringe pump (interfacial layer, Harvard Apparatus, Cambridge, MA, USA), and an Ultra 2800 positive displacement dispenser (shell, Nordson EFD). All printed and tested structures were cured sequentially for 1 h at 80 °C, 15 h at 100 °C, and 1 h at 220 °C.

Characterization: The dimensions of the printed structures were measured with a VHX-2000 optical microscope and a VH-Z20R 20×-200× optical zoom lens (Keyence, Osaka, Japan), which was calibrated before each session. The mechanical properties were measured on an Instron 5566 Universal Testing Machine with a constant crosshead speed of 10 mm s^{-1} (Instron, High Wycombe, United Kingdom). For the struts, a 10 N static load cell was used, while a 1000 N static load cell was used for the lattice structures and tensile tests. The struts were tested in three-point bending according to the ASTM D790-10 standard test method for flexural properties of unreinforced and reinforced plastics with a support span of 15 mm and support diameters of 2 mm, on a custom-built test rig. The lattices were tested in compression using polished steel plates to minimize friction. Tensile tests were performed on "Type V"-sized specimens according to the ASTM D638-10 standard test method for tensile properties of plastics. The displacement was measured with an Advanced Video Extensometer (Instron). The reported properties represented a mean of at least three samples.

Supporting Information

Supporting Information is available from the Wiley Online Library or from the author.

Acknowledgements

This work was supported by the National Science Foundation through the Harvard MRSEC through Grant # DMR-1420570. J.A.L. gratefully acknowledges partial support from the Vannevar Bush Faculty Fellowship Program sponsored by the Basic Research Office of the Assistant Secretary of Defense for Research and Engineering and funded by the Office of Naval Research Grant N00014-16-1-2823. The authors thank James C. Weaver for the assistance with SEM imaging. Finally, J.A.L. thanks the GETTYLAB for their generous donation in support of our research.

Conflict of Interest

Jennifer Lewis has cofounded a company, Voxel8 Inc., which focuses on multimaterial 3D printing. We have filed a patent on this work.

Keywords

3D printing, architected materials, core–shell, direct ink writing, energy absorption, fracture mechanics

Received: September 1, 2017
Revised: December 9, 2017
Published online:

[1] X. Zheng, H. Lee, T. H. Weisgraber, M. Shusteff, J. DeOtte, E. B. Duoss, J. D. Kuntz, M. M. Biener, Q. Ge, J. A. Jackson, S. O. Kucheyev, N. X. Fang, C. M. Spadaccini, *Science* **2014**, *344*, 1373.
[2] L. R. Meza, S. Das, J. R. Greer, *Science* **2014**, *345*, 1322.
[3] B. G. Compton, J. A. Lewis, *Adv. Mater.* **2014**, *26*, 5930.
[4] E. B. Duoss, T. H. Weisgraber, K. Hearon, C. Zhu, W. Small, T. R. Metz, J. J. Vericella, H. D. Barth, J. D. Kuntz, R. S. Maxwell, *Adv. Funct. Mater.* **2014**, *24*, 4905.
[5] J. T. Muth, P. G. Dixon, L. Woish, L. J. Gibson, J. A. Lewis, *Proc. Natl. Acad. Sci. USA* **2017**, *114*, 1832.
[6] L. R. Meza, A. J. Zelhofer, N. Clarke, A. J. Mateos, D. M. Kochmann, J. R. Greer, *Proc. Natl. Acad. Sci. USA* **2015**, *112*, 11502.
[7] R. L. Truby, J. A. Lewis, *Nature* **2016**, *540*, 371.
[8] U. G. Wegst, H. Bai, E. Saiz, A. P. Tomsia, R. O. Ritchie, *Nat. Mater.* **2015**, *14*, 23.
[9] S. Weiner, H. D. Wagner, *Annu. Rev. Mater. Sci.* **1998**, *28*, 271.
[10] P. Fratzl, H. Gupta, E. Paschalis, P. Roschger, *J. Mater. Chem.* **2004**, *14*, 2115.
[11] R. O. Ritchie, *Nat. Mater.* **2011**, *10*, 817.
[12] M. E. Launey, M. J. Buehler, R. O. Ritchie, *Annu. Rev. Mater. Res.* **2010**, *40*, 25.
[13] T. Stanković, J. Mueller, P. Egan, K. Shea, *J. Mech. Des.* **2015**, *137*, 111405.
[14] M. P. Bendsoe, O. Sigmund, *Topology Optimization: Theory, Methods, and Applications*, Springer-Verlag Berlin Heidelberg, Berlin, Germany **2013**.
[15] T. Stanković, J. Mueller, K. Shea, *Addit. Manuf.* **2017**, *17*, 67.
[16] T. A. Schaedler, A. J. Jacobsen, A. Torrents, A. E. Sorensen, J. Lian, J. R. Greer, L. Valdevit, W. B. Carter, *Science* **2011**, *334*, 962.
[17] M. F. Ashby, T. Evans, N. A. Fleck, J. Hutchinson, H. Wadley, L. Gibson, *Metal Foams: A Design Guide*, Butterworth-Heinemann, Oxford, United Kingdom, **2000**.
[18] L. Montemayor, J. Greer, *J. Appl. Mech.* **2015**, *82*, 071012.
[19] J. E. Smay, J. Cesarano, J. A. Lewis, *Langmuir* **2002**, *18*, 5429.
[20] C. Minas, D. Carnelli, E. Tervoort, A. R. Studart, *Adv. Mater.* **2016**, *28*, 9993.
[21] M. O'Masta, L. Dong, L. St-Pierre, H. Wadley, V. Deshpande, *J. Mech. Phys. Solids* **2017**, *98*, 271.
[22] T. Tancogne-Dejean, A. B. Spierings, D. Mohr, *Acta Mater.* **2016**, *116*, 14.
[23] A. G. Evans, M. He, V. S. Deshpande, J. W. Hutchinson, A. J. Jacobsen, W. B. Carter, *Int. J. Impact Eng.* **2010**, *37*, 947.
[24] Y. Liu, T. A. Schaedler, A. J. Jacobsen, X. Chen, *Composites, Part B* **2014**, *67*, 39.
[25] X. Zheng, W. Smith, J. Jackson, B. Moran, H. Cui, D. Chen, J. Ye, N. Fang, N. Rodriguez, T. Weisgraber, *Nat. Mater.* **2016**, *15*, 1100.
[26] M. A. Meyers, J. McKittrick, P.-Y. Chen, *Science* **2013**, *339*, 773.

[27] J. R. Greer, J. T. M. De Hosson, *Prog. Mater Sci.* **2011**, *56*, 654.
[28] A. Jackson, J. Vincent, R. Turner, *Proc. R. Soc. London, Ser. B* **1988**, *234*, 415.
[29] M. A. Dawson, L. J. Gibson, *Int. J. Solids Struct.* **2007**, *44*, 1145.
[30] P. F. Egan, S. J. Ferguson, K. Shea, *J. Mech. Des.* **2017**, *139*, 061401.
[31] J. A. Lewis, *Adv. Funct. Mater.* **2006**, *16*, 2193.
[32] G. Giannakopoulos, K. Masania, A. Taylor, *J. Mater. Sci.* **2011**, *46*, 327.
[33] H. Tippur, A. Rosakis, *Exp. Mech.* **1991**, *31*, 243.
[34] P. Fratzl, H. S. Gupta, F. D. Fischer, O. Kolednik, *Adv. Mater.* **2007**, *19*, 2657.
[35] A. J. Kinloch, *Fracture behaviour of polymers*, Springer Science & Business Media, Berlin, Germany **2013**.
[36] B. Johnsen, A. Kinloch, R. Mohammed, A. Taylor, S. Sprenger, *Polymer* **2007**, *48*, 530.
[37] K. A. Hing, *Philos. Trans. R. Soc., A* **2004**, *362*, 2821.
[38] E. Munch, M. E. Launey, D. H. Alsem, E. Saiz, A. P. Tomsia, R. O. Ritchie, *Science* **2008**, *322*, 1516.
[39] M. A. Meyers, P.-Y. Chen, A. Y.-M. Lin, Y. Seki, *Prog. Mater. Sci.* **2008**, *53*, 1.
[40] F. García Santamaría, M. Xu, V. Lousse, S. Fan, P. V. Braun, J. A. Lewis, *Adv. Mater.* **2007**, *19*, 1567.
[41] V. Deshpande, M. Ashby, N. Fleck, *Acta Mater.* **2001**, *49*, 1035.